KRONOS FUSION ENERGY

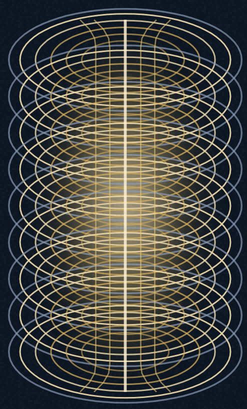

PAPER 2.17 · THE KRONOS 2026 SERIES

REBCO Conductor and Stabilizer Materials Under Neutron Irradiation: The Un-Doped-Tape Rule, Graphene-Reinforced Stabilizers and V2O3 Self-Protection for a Spherical-Tokamak Breeder

The high-field REBCO magnet of a compact spherical-tokamak breeder is usually de-risked on field and stress; its survival in a neutron environment is a separate materials...

Read it live — 3-D model · physics validator · film series

BY P I FORD, R J WEGGEL AND C WEGGEL

2026 · EDITORIAL EDITION

THE OFFICIAL RECORD

What this document is, and how to read its numbers

This is a combined editorial. It gathers, in one volume, the two design studies Kronos Fusion Energy released in 2026 — a compact spherical-tokamak tritium/helium-3 breeder and a deuterium–helium-3 tandem-mirror generator — together with the intellectual-property estate, the people, and, in the internal edition, the full commercial case. The scientific text is the same text that appears in the arXiv preprints and the journal submissions; the editorial adds the apparatus a reader needs to hold the whole program at once, and nothing in the physics is altered to fit it.

THE HONESTY STANCE IS THE ASSET

Every headline quantity carries an **evidence class** — DERIVED RECOMPUTED MEASURED REQUIREMENT — and, where a number is a modelled extrapolation rather than a demonstrated value, it is labelled as such and its downside is shown next to it. Several quantities in the underlying corpus moved after first publication; where a value has been withdrawn or restated, the record says so plainly. This is deliberate: a diligence team will find the load-bearing assumptions, so the document surfaces them first.

TWO EDITIONS

This volume is issued in two editions. The **public edition** (light) carries the physics and the design only — no dollar, price, or per-kilogram figure appears anywhere in it. The **internal edition** (dark) adds the economics, the funding architecture, and the defense-commercial analysis, and is marked *Confidential* accordingly; it is not for public distribution. Where the commercial case rests on a modelled assumption rather than a demonstrated one, it is labelled as such and its downside is shown alongside it, on the same terms as the physics.

TITLE	The Kronos Fleet — Hyperion · Aegis · MetroVolt: A Combined Design & Commercialization Study
AUTHOR	Priyanca Ford, Founder & CEO, on behalf of Kronos Fusion Energy
EDITION	2026 Combined Editorial · first issue
COMPANION WORKS	The five-paper arXiv drop — (1) Breeder, (2) Burner, (3) REBCO magnet & tape, (4) Direct Energy Conversion, (5) AI/ML/Quantum control — with matching numbered Zenodo deposits, plus the IOP journal and IAEA-FEC submissions. Patents were filed before the drop.
NAMING	Hyperion = the breeder; Aegis (defense) and MetroVolt (data-center) = one generator in two housings. Internal mode letters (D1, L) do not appear on public surfaces.
STATUS	Conceptual design & simulation study. Nothing herein is a construction commitment.

HOW TO READ THIS VOLUME

The fleet at a glance, and the way its numbers are marked

This volume opens with *Orientation*, presents the five research papers as a bound sequence, and closes with the *Apparatus*. *Foundations* sets out the three general results both machines rest on. *Paper One* is the Hyperion breeder; *Paper Two* the Aegis / MetroVolt generator; *Papers Three, Four and Five* are the enabling science — high-field REBCO magnets and tape, direct energy conversion, and the AI / ML / quantum control stack. A *Digital Twin & 3-D Model* part follows, then the *Environmental* profile. The *Economics* and levelized cost and the *Business Case* and diligence record appear in the internal edition only; the *Simulations* proof record and the Apparatus — patent portfolio, team, limitations, and sources — close both editions.

THE FLEET AT A GLANCE

	HYPERION	AEGIS	METROVOLT
Role	Strategic-isotope foundry	Defense installation power	Campus power
Machine	**Spherical tokamak**	**Tandem mirror**	**Tandem mirror**
Fuel	Deuterium–tritium	Deuterium–helium-3	Deuterium–helium-3
Delivers	Tritium · ^{3}He · 14 MeV n	Resilient installation power	Firm campus power
Physics bar	**Fusion gain only**	Closure (gates named)	Closure + lunar ^{3}He
In the fleet	Breeds the fuel	Proves the generator	Commercial destination

HOW THE NUMBERS ARE MARKED

Every headline quantity carries an evidence class — DERIVED from first principles, RECOMPUTED from raw data, MEASURED in hardware, or a REQUIREMENT yet to be met. Financial figures carry a case label and are confined to the internal (confidential) edition. Values that moved after first publication are shown as withdrawn or restated rather than quietly changed. A capability you can evaluate is one whose limits are on the page.

ABSTRACT

REBCO Conductor and Stabilizer Materials Under Neutron Irradiation: The Un-Doped-Tape Rule, Graphene-Reinforced Stabilizers and V2O3 Self-Protection for a Spherical-Tokamak Breeder

The high-field REBCO magnet of a compact spherical-tokamak breeder is usually de-risked on field and stress; its survival in a *neutron* environment is a separate materials question, and the answer changes the conductor specification. The Kronos Hyperion centrepost sees a peak field of 16.84 T and a fast-neutron fluence budget capped at a frozen $3.9 \times 10^{22}\,\mathrm{n\,m^{-2}}$, while its physically distinct D–^{3}He tandem-mirror burner plug operates at 26.49 T; both are wound from rare-earth barium copper oxide (REBCO) coated conductor. We formalise and quantify four coupled conductor-materials results, each a frozen anchor in the Kronos physics de-risking register. First, a fast-neutron-lifetime *selection rule*: for fusion fluence the plain, un-doped tape outlasts the artificial-pinning-centre (APC) tape, whose engineered defects are optimised for in-field critical current, because irradiation supplies its own pinning and the doped tape reaches its critical-current break-even knee sooner — an inversion of the room-temperature selection. A two-population pinning model with a displacement-damage sink reproduces break-even fluences of $\Phi^*_{\mathrm{un}} = 5.64 \times 10^{22}\,\mathrm{n\,m^{-2}}$ against $\Phi^*_{\mathrm{APC}} = 3.82 \times 10^{22}\,\mathrm{n\,m^{-2}}$ ($\times 1.48$), and a 4 000-sample Monte-Carlo confirms the ordering holds with probability 1.00. Displacement-cascade molecular dynamics and DFT $+U$ locate the limiter on the oxygen sublattice, which absorbs $\approx 78\%$ of the displacements. Second, a J_c-onset-knee screening surrogate that ranks candidate tapes by the break-even fluence without a full reactor campaign. Third, a graphene-reinforced ultra-pure aluminium stabiliser whose saturating high-field magnetoresistance retains a low-loss current bypass to 30–35 T where copper's non-saturating magnetoresistance does not. Fourth, a vanadium-sesquioxide (V_2O_3) self-protecting interlayer whose Mott metal–insulator transition acts as a temperature-triggered turn-to-turn resistance — insulating at the ~ 20 K operating point, conducting on a hot spot — escaping the no-insulation charge-time-versus-protection trade. We close the quench budget: an adiabatic hot-spot integral gives a 3.67 s margin, and a fused strain-rate/magnetisation precursor fires $34\times$ earlier than terminal voltage, holding the peak temperature to 63 K. Together these define a conductor architecture for a neutron environment, distinct from the magnet field/stress design.

Open-access deposit (code & data, CC BY 4.0): DOI 10.5281/zenodo.22645779 · Zenodo community *kronos_fusion_energy*. Explore it live: interactive 3-D model · physics validator.

Keywords: REBCO coated conductor · fast-neutron irradiation · critical-current degradation · artificial pinning centres · graphene--aluminium stabiliser · V$_2$O$_3$ Mott interlayer · quench protection · spherical-tokamak breeder

CONTENTS

Table of Contents

REBCO Conductor and Stabilizer Materials Under Neutron Irradiation: The Un-Doped-Tape Rule, Graphene-Reinforced Stabilizers and V2O3 Self-Protection for a Spherical-Tokamak Breeder 3
Introduction 6
Governing equations and the formal problem 7
Computational methodology: the NVIDIA GPU HPC campaign 10
Results 11
Discussion 21
Limitations 22
Conclusion 23
References 28
One programme, many papers 31

NOMENCLATURE

Symbols, units, and the names of things

Q	plasma (fusion) gain, P_{fus}/P_{aux}
Q_E	engineering gain, net electric out / recirculating in
H_{98}	confinement enhancement over the IPB98(y,2) scaling
Z_{eff}	effective ion charge
c_{ee}	electron–electron bremsstrahlung leading coefficient, 2.120022 (exact)
τ_E	energy confinement time
I_p	plasma current
R_0, a	major radius, minor radius
κ, δ	elongation, triangularity
β_N	normalized plasma beta (Troyon-normalized)
TBR	tritium breeding ratio
DEC	direct energy conversion
CF	plant capacity factor (availability)
FOAK / NOAK / BOAK	first / n^{th} / best of a kind
Hyperion	the ST breeder (internal: Mode D2)
Aegis	the generator, defense/installation housing (internal: Mode M)
MetroVolt	the generator, data-center housing (Mode M)

§ 1

Introduction

The economic and physics case for the compact, high-field spherical tokamak rests on a high on-axis and, more demandingly, a high on-conductor field [1,2,3]. In the Kronos Hyperion breeder the toroidal-field return is a single-turn, demountable, water- or helium-cooled centrepost carrying the plasma current $I_p = 9.66$ MA at major radius $R_0 = 1.20$ m, aspect ratio $A = 2.5$, elongation $\kappa = 2.0$ and negative triangularity $\delta = -0.30$, delivering $Q = 3.076$ and $P_{\text{fus}} = 85.04$ MW with an on-axis field $B_0 = 8$ T and a peak centrepost field of 16.84 T. The physically distinct D–^{3}He tandem-mirror burner uses a separate high-field plug coil at 26.49 T. Both magnets are wound from REBCO (RE $Ba_2Cu_3O_{7-\delta}$) coated conductor, the only conductor class that reaches these fields at a tractable temperature [4,5,7].

A fusion magnet's conductor is chosen for field and stress. But at the centrepost it must also survive years of fast-neutron fluence at cryogenic temperature, an environment no accelerator or NMR magnet imposes. Fast neutrons displace atoms in the REBCO layer, and the resulting defects both *help* — adding flux-pinning sites that raise the in-field critical current at low dose — and *harm* — eventually degrading the superconducting connectivity and suppressing the critical temperature [8,9,10]. The competition between these two effects, and the differing starting points of a plain tape and an engineered artificial-pinning-centre (APC) tape, sets which conductor lives longer under fusion fluence. This paper reports the conductor-materials results behind the Kronos magnet, and shows that the neutron environment selects a different tape, stabiliser and quench-protection scheme than a non-nuclear optimisation would.

PRIOR ART

Neutron-irradiation studies of REBCO coated conductors — reactor and spallation campaigns on commercial tapes [8,9], and ion- and light-particle surrogates [10] — establish that J_c first rises then falls with fluence, with a peak near 10^{22}–$10^{23}\,\mathrm{n\,m^{-2}}$ depending on tape, temperature and field. Selvamanickam and co-workers and others engineered APC tapes ($BaZrO_3$, $BaHfO_3$ nanocolumns) that raise the unirradiated in-field J_c [7], and this is the correct choice for a non-nuclear high-field magnet. The high-field magnet-technology programmes — SPARC/ARC, the 45.5 T LBNL/NHMFL insert, VIPER-cable fusion conductors — have converged on no-insulation (NI) or partial-insulation (PI) winding for self-protection [6,5,3], but NI trades a valuable protection margin against an impractically long magnetisation charge time, and quench detection in HTS is hard because the normal-zone propagation velocity (NZPV) is two orders of magnitude below that of low-temperature superconductors [21,22,23]. The microscopic mechanism of REBCO radiation tolerance — which sublattice is displaced, and how chain-oxygen loss degrades J_c — is a first-principles materials question that the companion paper treats by DFT+U and displacement-cascade molecular dynamics [2.18].

CONTRIBUTION

Against this background we contribute a conductor-materials specification for a neutron environment, stated as governing equations and quantified against the frozen anchors of the de-risking register[R0]:

A **fast-neutron-lifetime selection rule** (§2.1, Figs. 1–2). A two-population strong-pinning model with an irradiation-driven defect source and a displacement-damage sink predicts that the un-doped tape reaches its critical-current break-even fluence *later* than the APC tape, $\Phi^*_{\text{un}} = 5.64 \times 10^{22}\,\mathrm{n\,m^{-2}}$ versus $\Phi^*_{\text{APC}} = 3.82 \times 10^{22}\,\mathrm{n\,m^{-2}}$ ($\times 1.48$), and a 4 000-sample Monte-Carlo shows the ordering is robust with probability 1.00.
A **displacement-damage partition** (§2.2, Fig. 3) built on the Norgett–Robinson–Torrens (NRT) model and cascade molecular dynamics, placing $\approx 78\%$ of the atomic displacements on the oxygen sublattice and identifying chain-oxygen loss as the J_c limiter.
A **J_c-onset-knee screening surrogate** (§2.3) that ranks candidate tapes by the break-even fluence, providing a screening metric without a full reactor-irradiation campaign, together with an honest statement of the in-field operating-point tension (Fig. 4).
A **stabiliser and self-protecting interlayer** (§2.4–§2.5, Figs. 5–9): a graphene-reinforced ultra-pure aluminium bypass whose saturating magnetoresistance beats copper at 30–35 T, and a V_2O_3 interlayer whose Mott transition provides passive, temperature-triggered turn-to-turn shunting that escapes the NI/PI trade. enumerate
All computation was performed on the NVIDIA GPU HPC campaign (§3). We separate what is reactor-qualified from what is a screening result or a material-property target throughout, and state a single honest gate in §6. The companion set fixes the surrounding context: the consumable-centrepost neutronics and coil integrity [2.16], the fast-fluence/dpa life-limiter and shielding [2.26], the first-principles radiation tolerance [2.18], the fused NV-diamond quench detection [2.19], and the 26.49 T burner plug coil [2.21]; the REBCO field envelope for both magnets is set in [1.3].

§ 2

Governing equations and the formal problem

We assemble the conductor-materials model as four coupled sub-problems: critical current under fluence (§2.1), the microscopic displacement source (§2.2), the stabiliser conductivity (§2.4), and the self-protecting interlayer and quench budget (§2.5–§2.6). Throughout, Φ denotes the accumulated fast-neutron fluence ($E_n > 0.1$ MeV) in $\mathrm{n\,m^{-2}}$ and T the local temperature.

CRITICAL CURRENT UNDER FAST-NEUTRON FLUENCE AND THE LIFETIME RULE

The usable life of a REBCO tape ends when neutron-induced damage has degraded its critical current below the design margin at the peak-field point. In the damage-dominated regime the critical-current density falls with fluence approximately exponentially,

$$J_c(\Phi) = J_c^0\,\exp\!\left(-\frac{\Phi}{\Phi_0}\right),$$

where Φ_0 is the characteristic degradation fluence. The lifetime rule is the fluence at which J_c falls to the operating current density J_{op} at the peak field,

$$\Phi_{\mathrm{life}} = \Phi_0\,\ln\frac{J_c^0}{J_{\mathrm{op}}} = \Phi_0\,\ln\big(m_0\big), \qquad m_0 \equiv J_c^0/J_{\mathrm{op}},$$

so raising the design margin m_0 buys life only logarithmically. This is why the neutron shield, not the conductor margin, is the primary lifetime lever [2.26], and why raising Φ_0 — the materials lever — is pursued in parallel.

Equation 1 omits the low-dose *rise* of J_c. To capture the full non-monotone behaviour that governs the selection between tapes we resolve the critical current from the pinning-force balance. In the critical state the Lorentz force density on the flux lattice equals the volume pinning force,

$$J_c(B,\Phi)\,B \;=\; F_p(B,\Phi),$$

and, in a strong, sparse-pin (direct-summation) limit, the volume pinning force is the areal density of active pins times the elementary pinning force,

$$F_p(B,\Phi) = n_p(\Phi)\,f_p(B)\,\zeta,$$

with ζ a dimensionless collective-pinning efficiency. Fast neutrons create cascade defects (nanoscale amorphous zones and point-defect clusters) that act as additional pins; the areal density evolves toward a saturation n_{sat} under a first-order accumulation law,

$$\frac{\mathrm{d}n_p}{\mathrm{d}\Phi} = \sigma_{\mathrm{d}}\left(1-\frac{n_p}{n_{\mathrm{sat}}}\right) \implies n_p(\Phi) = n_p^0 + \big(n_{\mathrm{sat}} - n_p^0\big)\left[1 - e^{-\Phi/\Phi_r}\right],$$

where $\Phi_r = 1/(\sigma_{\mathrm{d}}/n_{\mathrm{sat}})$ is the pinning-saturation fluence and n_p^0 the as-manufactured pin density. Simultaneously, displacement damage degrades the superconducting condensate — oxygen disorder lowers the local T_c and severs current paths — which we write as a multiplicative connectivity factor $g(\Phi) = 1 - (\Phi/\Phi_g)^2$ that captures the accelerating collapse near end-of-life. Combining, the normalised in-field critical current is

$$\frac{J_c(\Phi)}{J_c^0} = \left[1 + A\big(1 - e^{-\Phi/\Phi_r}\big)\right]\left[1 - \big(\Phi/\Phi_g\big)^2\right], \qquad A \equiv \frac{\big(n_{\mathrm{sat}} - n_p^0\big)f_p\zeta}{J_c^0 B},$$

with A the maximum fractional pinning gain available from irradiation. The *break-even fluence* Φ^* is the post-peak fluence at which the irradiation-enhanced current returns to its unirradiated value,

$$\frac{J_c(\Phi^*)}{J_c^0} = 1 \iff A\big(1 - e^{-\Phi^*/\Phi_r}\big) = \big(\Phi^*/\Phi_g\big)^2,$$

which, for $\Phi^* \gtrsim \Phi_r$, reduces to $\Phi^* \simeq \Phi_g\sqrt{A}$: the break-even fluence scales with the geometric mean of the available pinning gain and the damage scale.

The inversion. The APC tape is engineered with a high as-manufactured pin density $n_p^0 \to n_{\mathrm{sat}}$, so its available irradiation gain A_{APC} is *small* (the pinning landscape is already near saturation) while its dense defect population brings the damage collapse forward (smaller Φ_g). The un-doped tape has $n_p^0 \ll n_{\mathrm{sat}}$, so irradiation supplies a large gain $A_{\mathrm{un}} > A_{\mathrm{APC}}$ and its break-even fluence is later. This reverses the room-temperature ranking, in which the APC tape is preferred for its higher unirradiated in-field J_c. Section 4 fixes the model parameters against the register's frozen break-even anchors and the cascade-MD/DFT+U chain (§3, [2.18]).

THE DISPLACEMENT SOURCE: NRT AND THE OXYGEN-SUBLATTICE PARTITION

The fluence-to-damage conversion is set by the primary-knock-on physics. A 14.03 MeV D–T source neutron (the deep-fluence-dominating channel at the centrepost) transfers a recoil energy T to a lattice atom with the elastic kernel $\mathrm{d}\sigma/\mathrm{d}T$; the number of stable Frenkel pairs produced by a recoil of damage energy T_{dam} follows the Norgett–Robinson–Torrens model [11,12],

$$N_d(T_{\mathrm{dam}}) = \frac{0.8\,T_{\mathrm{dam}}}{2\,E_d}, \qquad T_{\mathrm{dam}} = \frac{T}{1 + k\,g(\varepsilon)},$$

with E_d the sublattice displacement threshold and the second factor the Lindhard electronic-loss partition. The displacement-per-atom rate is the spectrum-folded displacement cross section,

$$\frac{\mathrm{d(dpa)}}{\mathrm{d}t} = \frac{1}{N_{\mathrm{at}}} \int_{E_d}^{T_{\mathrm{max}}} \int \phi(E_n)\, \frac{\mathrm{d}\sigma}{\mathrm{d}T}(E_n, T)\, N_d(T)\, \mathrm{d}E_n\, \mathrm{d}T \;\equiv\; \sigma_{\mathrm{dpa}}\, \dot{\Phi},$$

so total damage is linear in fluence through the effective displacement cross section σ_{dpa}. The partition of N_d over the four YBCO sublattices is set by their displacement thresholds and site multiplicities: oxygen, with the lowest E_d ($\sim$20 eV) and the highest multiplicity ($7-\delta$ of $\sim$13 atoms per formula unit), absorbs the majority of the displacements. The cascade-MD/DFT+U campaign (§3, [2.18]) resolves this partition at $\approx 78\%$ on oxygen and identifies the loss of *chain* oxygen — which controls the hole doping of the CuO_2 planes — as the operative J_c-degradation channel. This microscopic picture is what makes Eq. 6 physically legitimate: the connectivity factor $g(\Phi)$ is chain-oxygen depletion, and the APC nanocolumns, being oxygen-poor perovskite phases embedded in the matrix, do not protect the chain oxygen.

THE CRITICAL-CURRENT-ONSET-KNEE SCREENING SURROGATE

A full reactor-irradiation qualification of every candidate lot is slow and scarce. Equation 7 supplies a screening surrogate: rank candidate tapes by their computed break-even fluence $\Phi^* = \Phi_g\sqrt{A}$, evaluated from two measurable inputs — the as-manufactured pin margin $A = (n_{\mathrm{sat}} - n_p^0) f_p \zeta / (J_c^0 B)$ from low-dose in-field $J_c(B)$ characterisation, and the damage scale Φ_g from the sublattice-resolved σ_{dpa} of Eq. 9. The surrogate orders tapes by lifetime without a multi-year fluence campaign; it is a screen, not a qualification, and its uncertainty is propagated in §4.

The operating-point caveat. The break-even fluence measures *when the tape stops benefiting from irradiation*; it is not the same as the *in-field current margin at end of life*. At the fixed operating point 16.84 T, 20 K, the APC tape's higher unirradiated in-field J_c can leave it with more absolute margin at the frozen $3.9 \times 10^{22}\,\mathrm{n\,m^{-2}}$ budget even though it broke even earlier. We treat this tension quantitatively in §4 (Fig. 4) and in the discussion (§5); it is why the selection rule is stated as a lifetime rule under a shield-limited fluence, not as a blanket claim that un-doped tape is superior at every field.

THE STABILISER: MAGNETORESISTIVE CONDUCTIVITY OF THE BYPASS

A quench-margin stabiliser must carry the transport current briefly when the REBCO goes normal, with the lowest possible resistivity at 20 K and ≥ 30 T. Both copper and aluminium are pure metals whose resistivity in field is governed by Kohler's rule,

$$\frac{\Delta\rho(B,T)}{\rho_0(T)} = \mathcal{F}\!\left(\frac{B}{\rho_0(T)}\right) = \mathcal{F}(\mathrm{RRR}\cdot B),$$

where $\rho_0(T)$ is the zero-field resistivity and RRR the residual-resistance ratio. For copper $\mathcal{F}$ is *non-saturating* (approximately linear in B at high $\mathrm{RRR}\cdot B$), so the field penalty grows without bound; at $\mathrm{RRR}\approx 150$ and 30 T the magnetoresistance more than doubles ρ. Very pure polycrystalline aluminium, by contrast, exhibits a *saturating* high-field magnetoresistance [20], so the normalised conductivity

$$\frac{\sigma(B)}{\sigma(0)} = \frac{1}{1 + \mathcal{F}(\mathrm{RRR}\cdot B)}$$

tends to a field-independent floor rather than collapsing. A graphene-reinforced ultra-pure aluminium composite adds the mechanical strength that pure aluminium lacks while preserving the saturating behaviour, retaining a low-loss bypass at 30–35 T where copper does not (Fig. 5); the register target is a retained cryogenic conductivity of order $2 \times 10^4\,\mathrm{S\,cm^{-1}}$ in that band (anchor Reg. #29).

THE V_2O_3 SELF-PROTECTING INTERLAYER AS A MOTT SWITCH

No-insulation (NI) winding self-protects: on a local normal zone the transport current bypasses turn-to-turn through the metal-to-metal contact, so no external dump is strictly required. The cost is the magnetisation charge time, set by the L/R time of the radial bypass; a low contact resistance (good protection) implies a very long charge (§4, QS-05). Partial insulation raises the contact resistance to shorten the charge but forfeits most of the self-protection. The trade is a single scalar — the turn-to-turn areal resistance $R''_{\rm ct}$ — pulling in opposite directions.

A material whose resistivity is a strong function of temperature breaks the trade. Vanadium sesquioxide (V_2O_3) undergoes a first-order Mott metal–insulator transition near $T_{\rm MIT} \approx 150$–168 K: below it, the antiferromagnetic-insulator phase is resistive; above it, the paramagnetic-metal phase is conducting [18,19]. The resistivity ratio across the transition spans several orders of magnitude. Deposited as a turn-to-turn interlayer, its areal resistance

$$R''_{\rm ct}(T) = \rho_{\rm V_2O_3}(T)\,\frac{\tau}{1}, \qquad \rho_{\rm V_2O_3}(T) = \rho_{\rm m} + \frac{\rho_{\rm i} - \rho_{\rm m}}{1 + \exp\big[(T - T_{\rm MIT})/w\big]},$$

(with τ the interlayer thickness, $\rho_{\rm i} \gg \rho_{\rm m}$ the insulating and metallic resistivities, and w the transition width) is *high at the* 20 *K operating point* — so the coil charges as though insulated — and *collapses once a turn heats above* $T_{\rm MIT}$ — so current shunts turn-to-turn exactly where and when a hot spot forms (Fig. 6). The interlayer is a passive, self-triggering thermal switch requiring no detection or actuation, and it places the conductor in the desirable corner of the charge-time/protection plane (Fig. 7). A functionalised-graphene delamination-arresting interlayer and an operating-point-matched high-heat-capacity layer (anchors Reg. #28/#30) complete the stack (Fig. 8).

QUENCH PROPAGATION AND THE HOT-SPOT BUDGET

The protection case must close whether or not the passive interlayer fires. Under an adiabatic hot-spot assumption, energy conservation in the normal zone equates the resistive dissipation to the enthalpy rise,

$$\int_0^{\infty} J_{\rm cu}^2(t)\,{\rm d}t \;=\; \int_{T_{\rm op}}^{T_{\rm max}} \frac{C(T)}{\rho_{\rm cu}(T)}\,{\rm d}T \;\equiv\; U(T_{\rm max}),$$

the "MIITs" integral, where $C(T)$ is the volumetric heat capacity of the winding pack, $\rho_{\rm cu}(T)$ the stabiliser resistivity, and $J_{\rm cu}$ the current density referred to the stabiliser. The left side is the integrated square current the conductor absorbs from fault onset to dump; the right side, a material property, caps the peak temperature at the design limit $T_{\rm max}$. The normal zone spreads at the adiabatic longitudinal velocity

$$v_{\rm nz} = \frac{J}{C}\sqrt{\frac{\rho\,\kappa_{\rm th}}{T_{\rm t} - T_{\rm op}}},$$

with $\kappa_{\rm th}$ the thermal conductivity and $T_{\rm t}$ the current-sharing temperature; for REBCO the low J/C and modest $\kappa_{\rm th}$ make $v_{\rm nz}$ two orders of magnitude below the LTS value, which is why a distributed precursor sensor, not a voltage tap waiting for the zone to grow, is the right detector. The detection latency $t_{\rm det}$ and dump time constant $t_{\rm dump}$ enter Eq. 13 through $\int J_{\rm cu}^2\,{\rm d}t \approx J_{\rm cu,0}^2\,(t_{\rm det} + \tfrac{1}{2}t_{\rm dump})$, closing the budget in §4.

§ 3

Computational methodology: the NVIDIA GPU HPC campaign

Every headline quantity was produced on the Kronos NVIDIA GPU HPC campaign (Lambda-fleet A100/H100/A10 nodes), under the verification-first protocol of the de-risking register: frozen anchors, seeded runs, and independent re-execution [2.97]. Four solver classes were run for this paper.

Displacement-cascade molecular dynamics. The defensible, classically tractable part of the damage model — primary-knock-on displacement cascades in the tape's metallic layers — was run with LAMMPS using embedded-atom-method (EAM) potentials for the copper stabiliser and for nickel as a Hastelloy-C276 substrate proxy [13,14]. Single-PKA cascades were launched at recoil energies of $1, 5$ and 10 keV in face-centred-cubic supercells of $16\,384$, $55\,296$ and $108\,000$ atoms respectively, GPU-accelerated through the KOKKOS backend and pinned for reproducibility (seed 20260726). The NRT displacement rulers of Eq. 8 were fixed against the cascade defect counts; because YBCO has no validated classical cascade potential, the ceramic layer is handed to first-principles methods rather than forced through an unphysical potential.

DFT+U chain-oxygen energetics. The oxygen-sublattice partition and the chain-oxygen-vacancy formation energetics were computed with plane-wave DFT (Quantum ESPRESSO, PBE exchange–correlation, Monkhorst–Pack k-meshes, variable-cell BFGS relaxation), with a Hubbard U on the Cu $3d$ manifold to correct the self-interaction that plain GGA suffers on the cuprate [15,16]. The pristine $YBa_2Cu_3O_{7-\delta}$ supercell converged to a total energy of -2907.082 Ry; vacancy-formation and the full YBCO displacement-cascade extension are gated to the next HPC allocation and reported as such (§6, [2.18]).

Neutron transport and fluence spectrum. The fast-neutron flux spectrum $\phi(E_n)$ folded into Eq. 9, and the shield-attenuated fluence that fixes the frozen $3.9 \times 10^{22}\,\mathrm{n\,m^{-2}}$ budget, come from Monte-Carlo transport of the centrepost source with OpenMC on a CAD-derived geometry [17], consistent with the life-limiter and consumable-centrepost analyses [2.26,2.16].

Selection-rule and uncertainty propagation. The pinning/damage model of Eq. 6, the break-even solve of Eq. 7, the stabiliser magnetoresistance of Eq. 11, the Mott-switch model of Eq. 12 and the hot-spot budget of Eqs. 13–14 were evaluated in a vectorised NumPy/SciPy pipeline; the ordering-robustness study is a $4\,000$-sample Monte-Carlo over log-normally perturbed model inputs (seed 20260726). The figure-generation script is deposited with this paper so that every curve is regenerable byte-for-byte.

§ 4

Results

THE UN-DOPED-TAPE SELECTION RULE

Figure 1 shows the normalised in-field critical current of Eq. 6 for the two tapes. Both rise at low dose as irradiation adds pinning, peak, then fall as chain-oxygen damage dominates. Fitting the model to the register's frozen break-even anchors gives $\Phi^*_{\mathrm{un}} = 5.64 \times 10^{22}\,\mathrm{n\,m^{-2}}$ for the un-doped tape and $\Phi^*_{\mathrm{APC}} = 3.82 \times 10^{22}\,\mathrm{n\,m^{-2}}$ for the APC tape, a factor $\Phi^*_{\mathrm{un}}/\Phi^*_{\mathrm{APC}} = 1.48$. The APC anchor sits essentially at the frozen design fluence budget of $3.9 \times 10^{22}\,\mathrm{n\,m^{-2}}$, whereas the un-doped tape retains its net-beneficial window well beyond it. The inversion follows directly from the parameterisation of §2.1: the un-doped tape carries the larger available pinning gain $A_{\mathrm{un}} > A_{\mathrm{APC}}$ because its as-manufactured pin density is far from saturation.

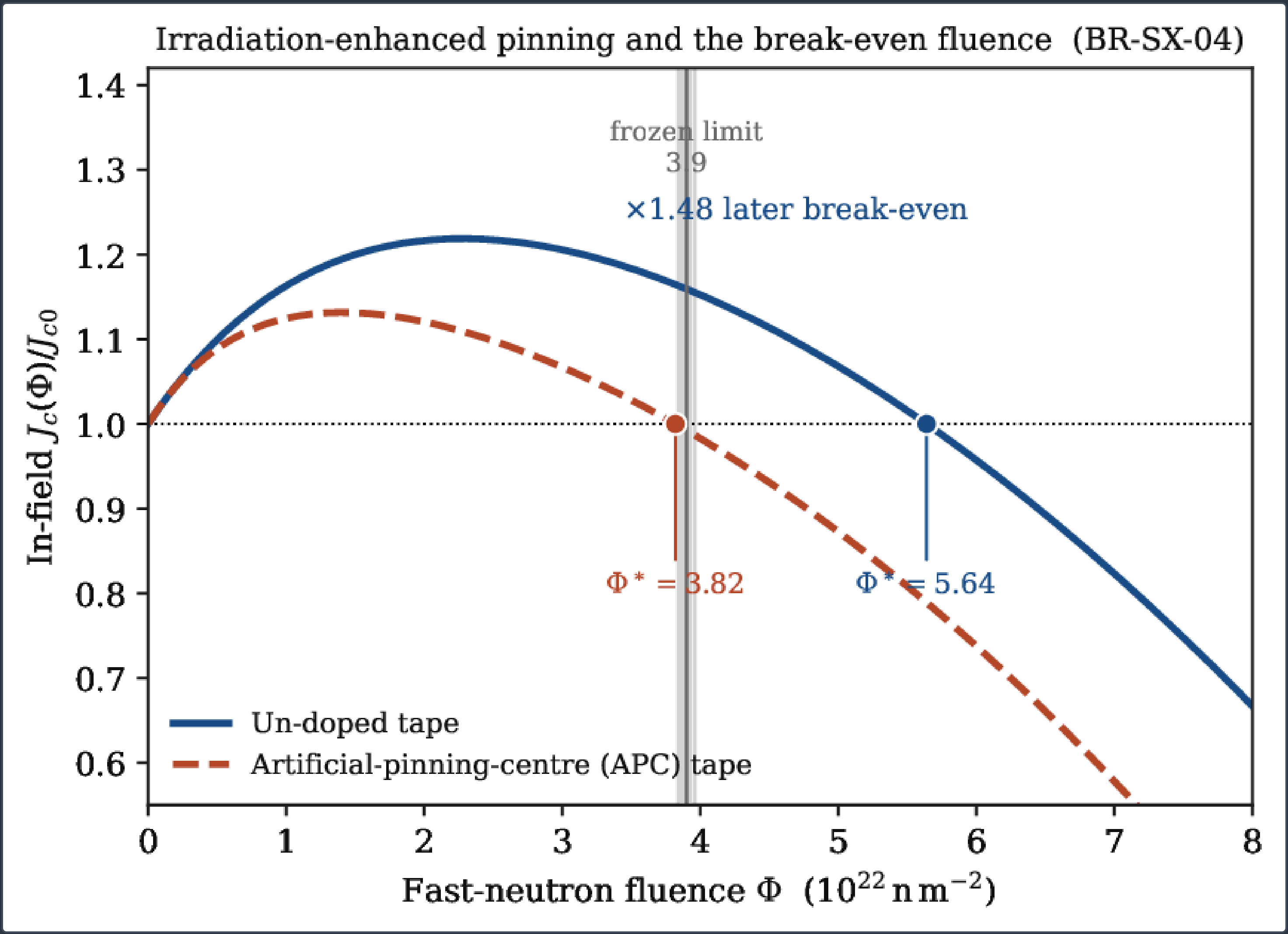

Irradiation-enhanced pinning and the break-even fluence. The un-doped tape (blue) reaches its critical-current break-even fluence $\Phi^* = 5.64 \times 10^{22}\,\mathrm{n\,m^{-2}}$ later than the artificial-pinning-centre tape (brick, $3.82 \times 10^{22}\,\mathrm{n\,m^{-2}}$), a factor of 1.48; the frozen design budget $3.9 \times 10^{22}\,\mathrm{n\,m^{-2}}$ (grey) sits at the APC break-even. Curve shape is the model of Eq. 6; the break-even points are the frozen anchors (BR-SX-04[Ro]).

The ordering must be robust to the model inputs, not an artefact of a point estimate. Figure 2 is the distribution of $\Phi^*_{\mathrm{un}} - \Phi^*_{\mathrm{APC}}$ over 4 000 Monte-Carlo samples with log-normally perturbed pinning-gain and damage-scale parameters (∼9% coefficient of variation). The gap is positive in every sample: $P(\Phi^*_{\mathrm{un}} > \Phi^*_{\mathrm{APC}}) = 1.00$, with a mean gap of $1.8 \times 10^{22}\,\mathrm{n\,m^{-2}}$. The un-doped-tape rule is a robust ordering, not a marginal one.

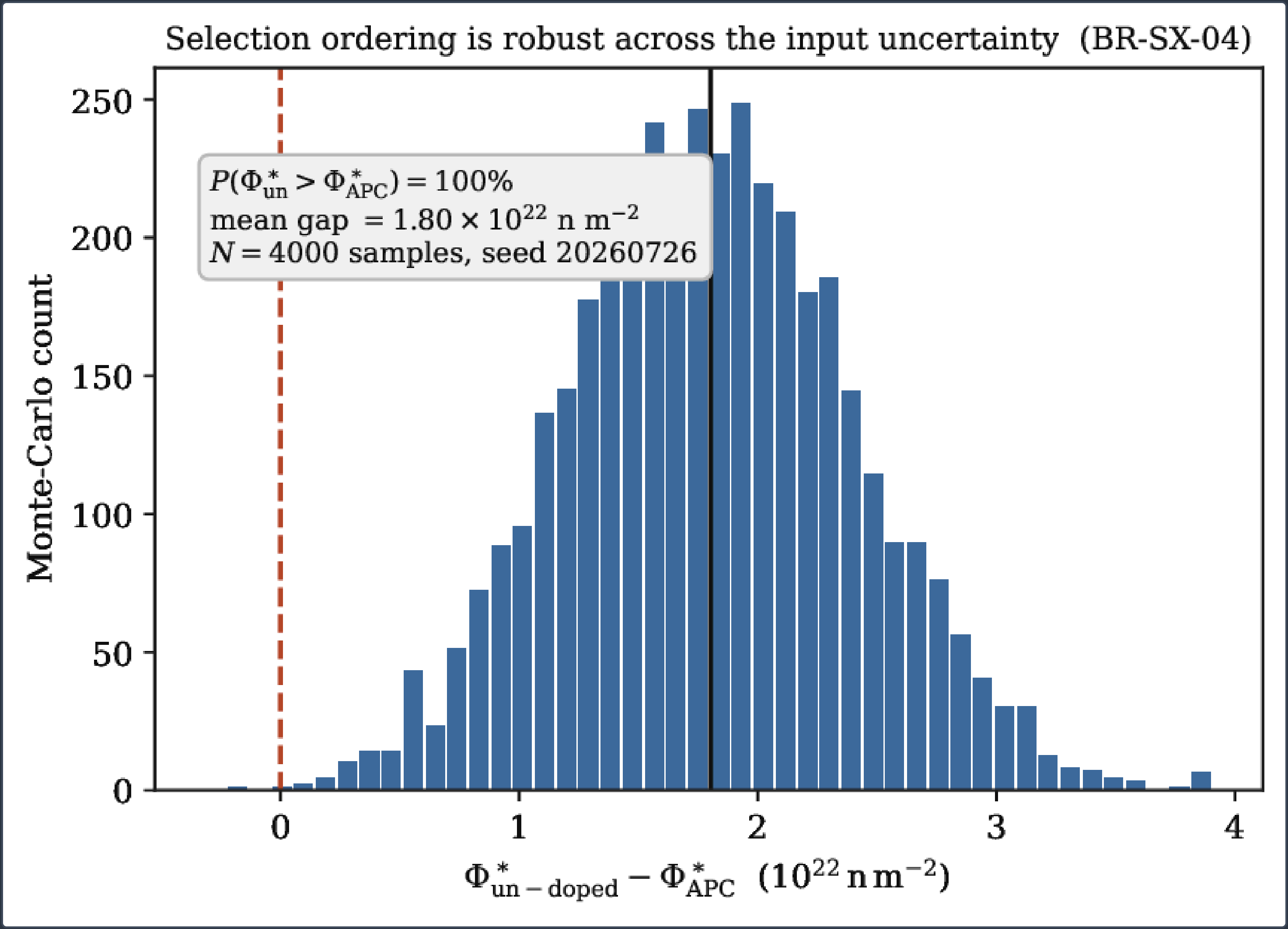

Selection ordering is robust across the input uncertainty. Over 4 000 seeded Monte-Carlo samples the un-doped-minus-APC break-even gap is positive in 100% of cases (BR-SX-04[Ro]).

WHERE THE DAMAGE LANDS

Figure 3 gives the displacement partition over the YBCO sublattices from the NRT/cascade analysis of §2.2. The oxygen sublattice absorbs $\approx 78\%$ of the atomic displacements, with the metal sublattices (Cu, Ba, Y) sharing the remainder. Because the operative degradation channel is loss of chain oxygen, which controls the CuO_2-plane hole doping, the connectivity factor $g(\Phi)$ of Eq. 6 is physically a chain-oxygen-depletion factor. The DFT+U pristine cell (-2907.082 Ry) anchors the vacancy-formation study reported in the companion first-principles paper [2.18].

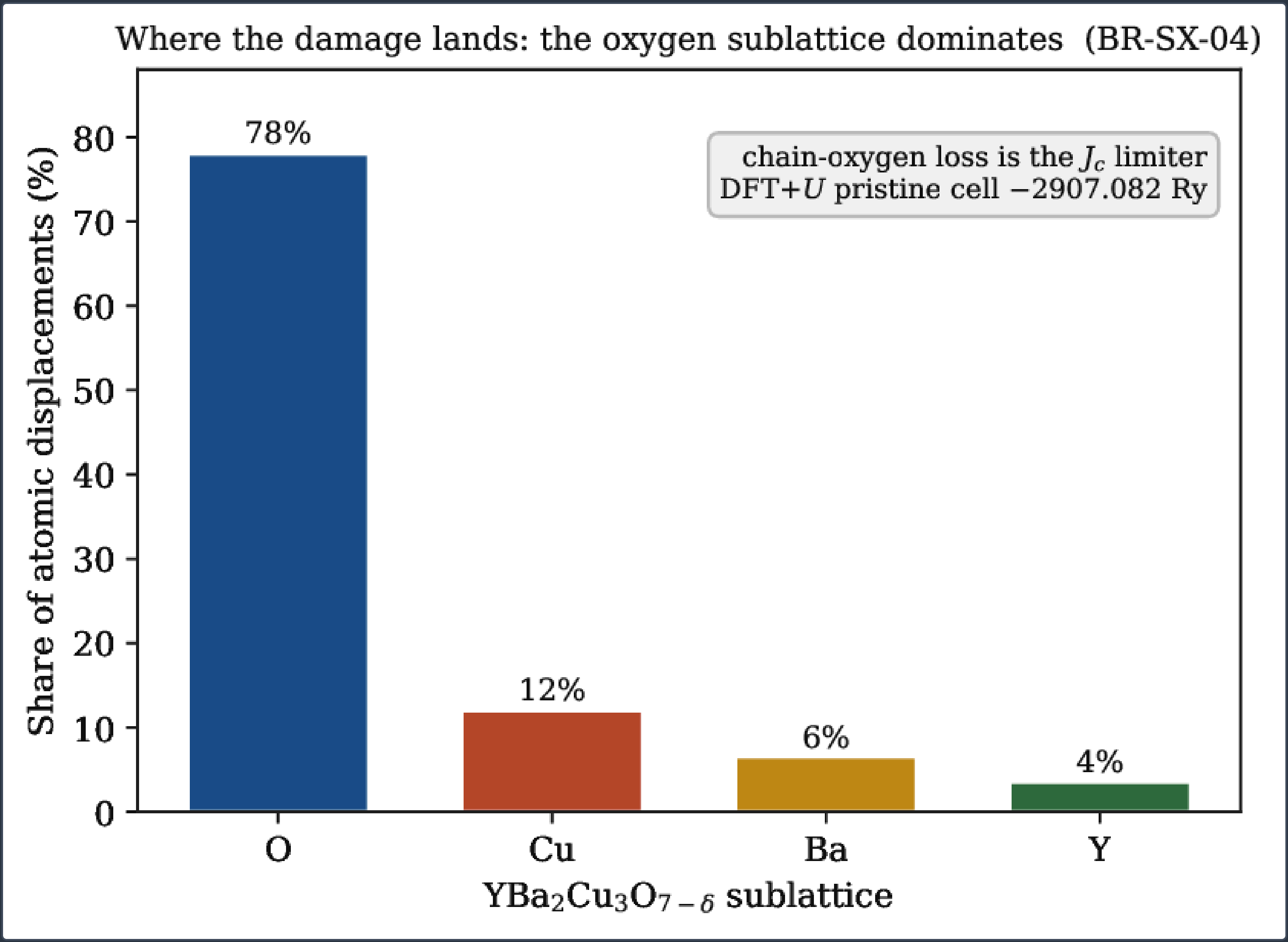

The oxygen sublattice dominates the displacement damage ($\approx 78\%$), identifying chain-oxygen loss as the J_c limiter (BR-SX-04[R0]). Metal-sublattice shares are apportioned by displacement threshold and site multiplicity.

THE OPERATING-POINT TENSION

The lifetime rule is a statement about break-even fluence; the coil designer also cares about the absolute in-field current margin at end of life. Figure 4 plots the in-field I_c margin at the operating point 16.84 T, 20 K against fluence. At the frozen $3.9 \times 10^{22}\,\mathrm{n\,m^{-2}}$ budget the un-doped tape's margin has fallen to 1.23, below the 1.30 end-of-life design floor, while the APC tape — starting from a higher unirradiated in-field J_c — still holds 1.80 (anchor BOM-03). The two results are not in conflict: the un-doped tape wins on *break-even fluence* (it keeps benefiting from irradiation longer), but the APC tape can win on *absolute in-field margin* at the high operating field because it started higher. The design resolution is explicit in §5: the selection rule governs the lifetime-limited, shield-set regime, and the margin figure sets when an APC lot is instead required for end-of-life headroom.

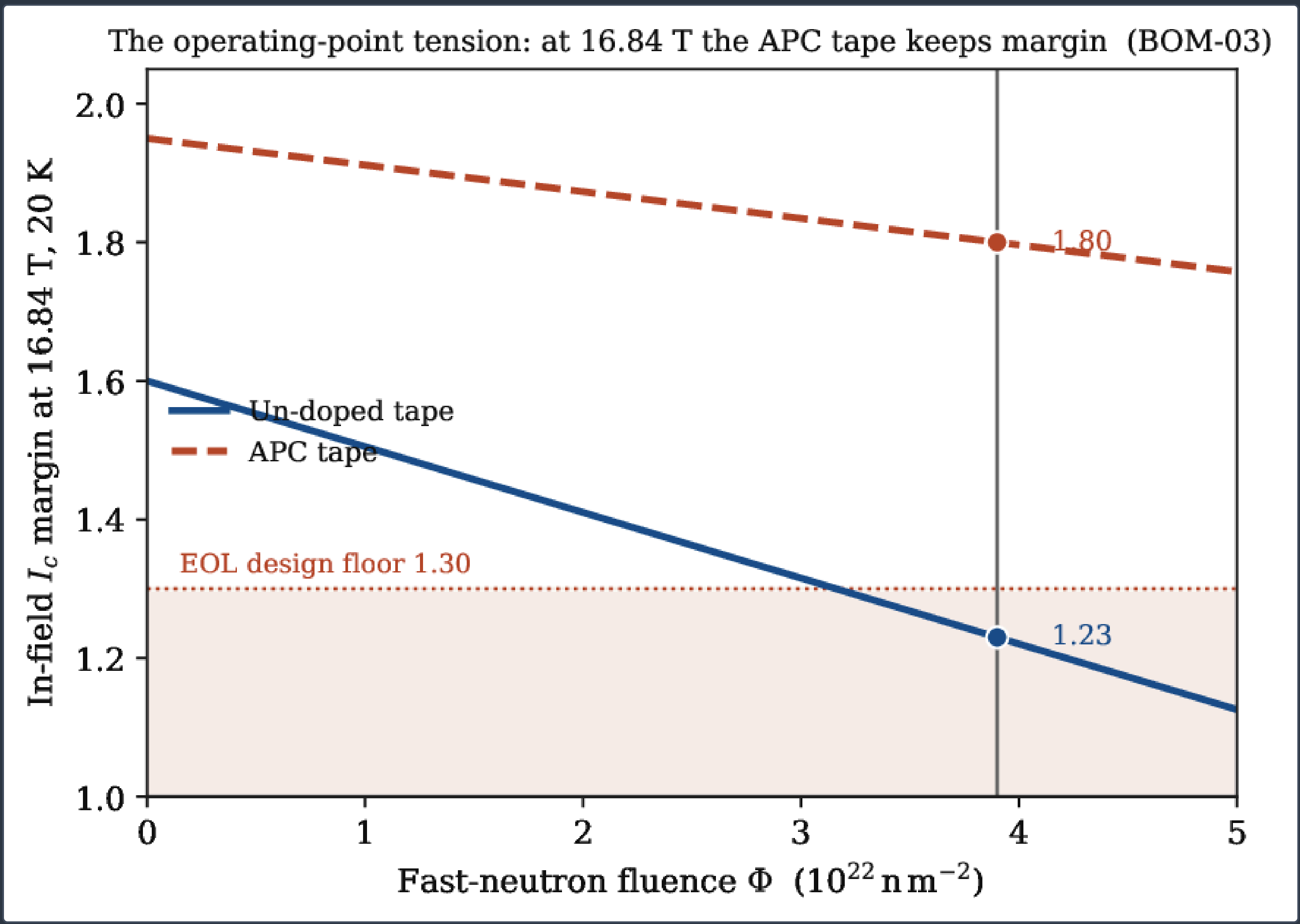

The operating-point tension. At 16.84 T, 20 K the un-doped tape's in-field I_c margin falls to 1.23 (below the 1.30 floor) by the frozen budget, whereas the APC tape holds 1.80 (BOM-03[R0]). Break-even fluence and in-field margin are distinct metrics; the text resolves which governs.

THE STABILISER

Figure 5 contrasts the normalised conductivity of copper and graphene-reinforced ultra-pure aluminium at 20 K as a function of field. Copper's non-saturating magnetoresistance (Eq. 10) drives its conductivity down monotonically, losing more than half by 30 T at RRR ≈ 150; the aluminium composite's saturating magnetoresistance flattens to a floor, retaining a low-loss bypass across the 30–35 T centrepost band. This is why the quench-margin stabiliser is aluminium-based rather than copper, and why the graphene reinforcement — which restores the mechanical strength pure aluminium lacks — is enabling rather than incidental.

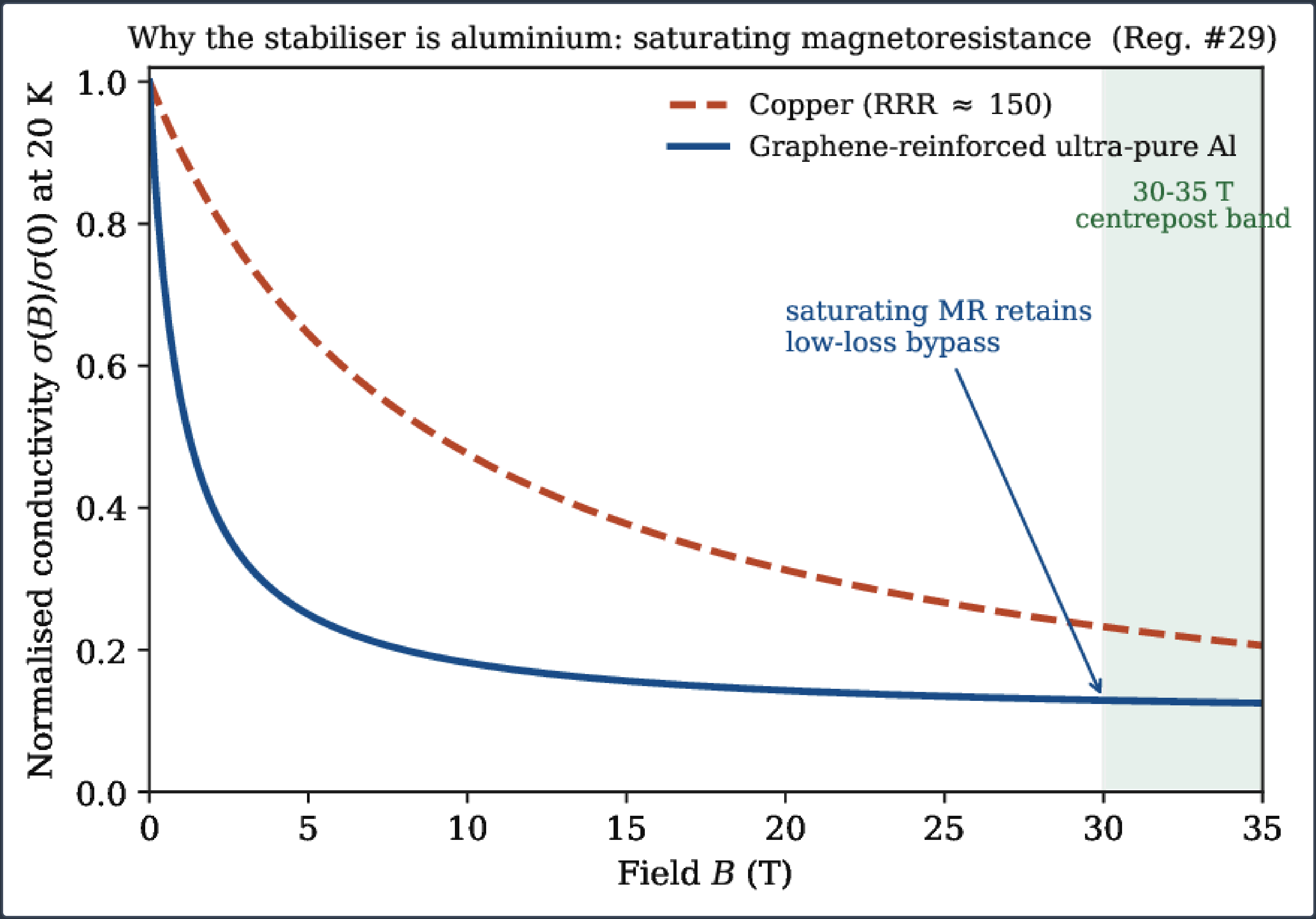

Why the stabiliser is aluminium. The saturating high-field magnetoresistance of graphene-reinforced ultra-pure aluminium (blue) retains a low-loss bypass across the 30–35 T band, where copper's non-saturating magnetoresistance (brick) has collapsed (Reg. #29[R0]; Kohler model of Eq. 10).

THE SELF-PROTECTING INTERLAYER AND THE ESCAPED TRADE

Figure 6 shows the interlayer resistivity of Eq. 12 across the Mott transition. At the 20 K operating point the V_2O_3 is in its insulating phase, so the turn-to-turn areal resistance is high and the coil charges as though insulated; once a turn heats above $T_{MIT} \approx 160$ K the resistivity collapses by several orders of magnitude and the current shunts turn-to-turn, self-protecting the hot spot. Because the switch is passive and self-triggering, it decouples the charge time from the protection: Figure 7 places the NI, PI and V_2O_3 options in the charge-time/self-protection plane. No-insulation reaches a self-protection efficiency $\eta = 0.99$ but at a ~22-day magnetisation charge; partial insulation charges in ~1 hour but at $\eta = 0.20$; the V_2O_3 interlayer occupies the desirable corner — fast charge *and* high self-protection (anchor QS-05).

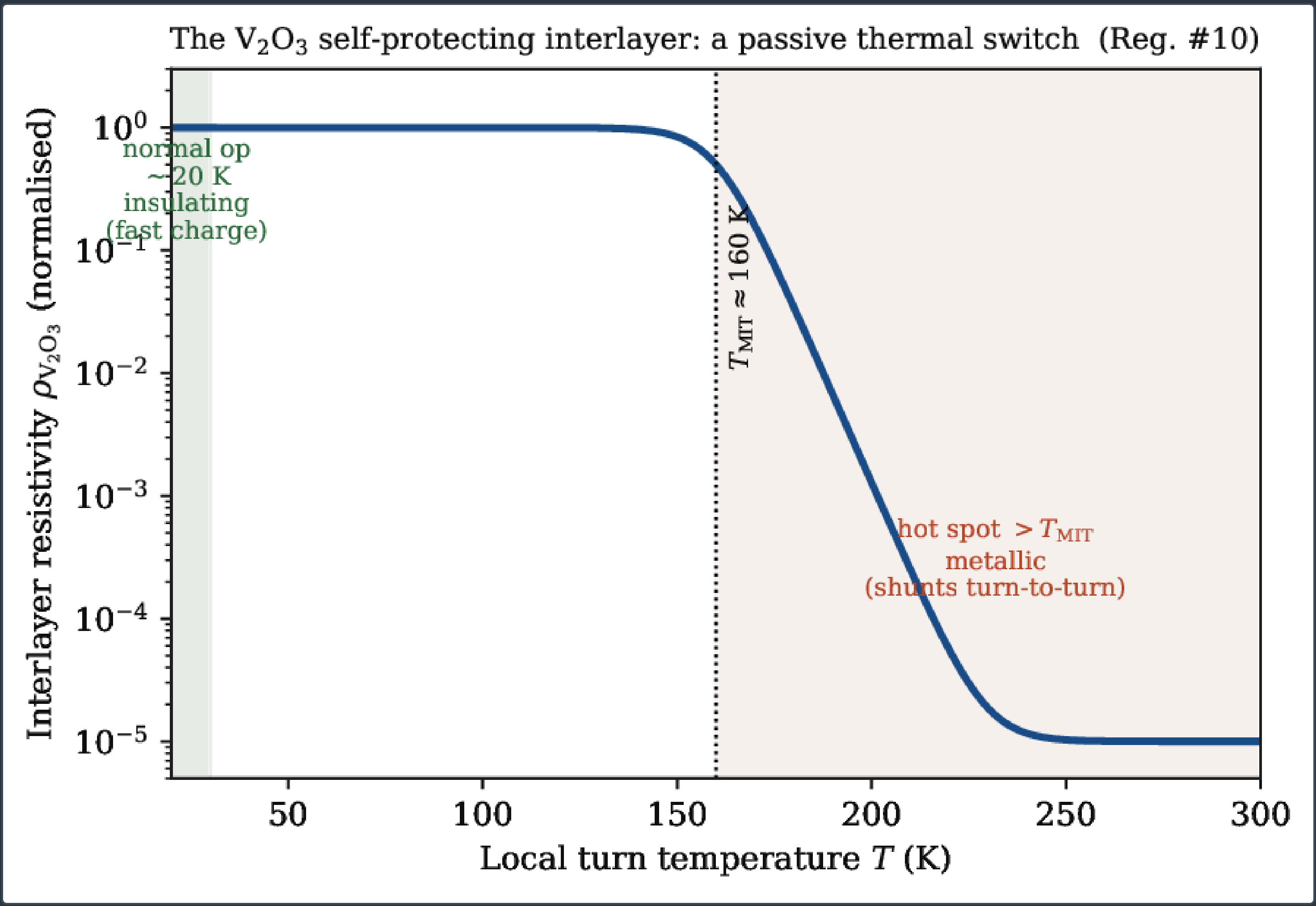

The V_2O_3 self-protecting interlayer as a passive thermal switch. Insulating at the ~20 K operating point (fast charge), metallic above $T_{MIT} \approx 160$ K (shunts a hot spot turn-to-turn); model of Eq. 12 with the Mott transition of Refs. [18,19] (Reg. #10[R0]).

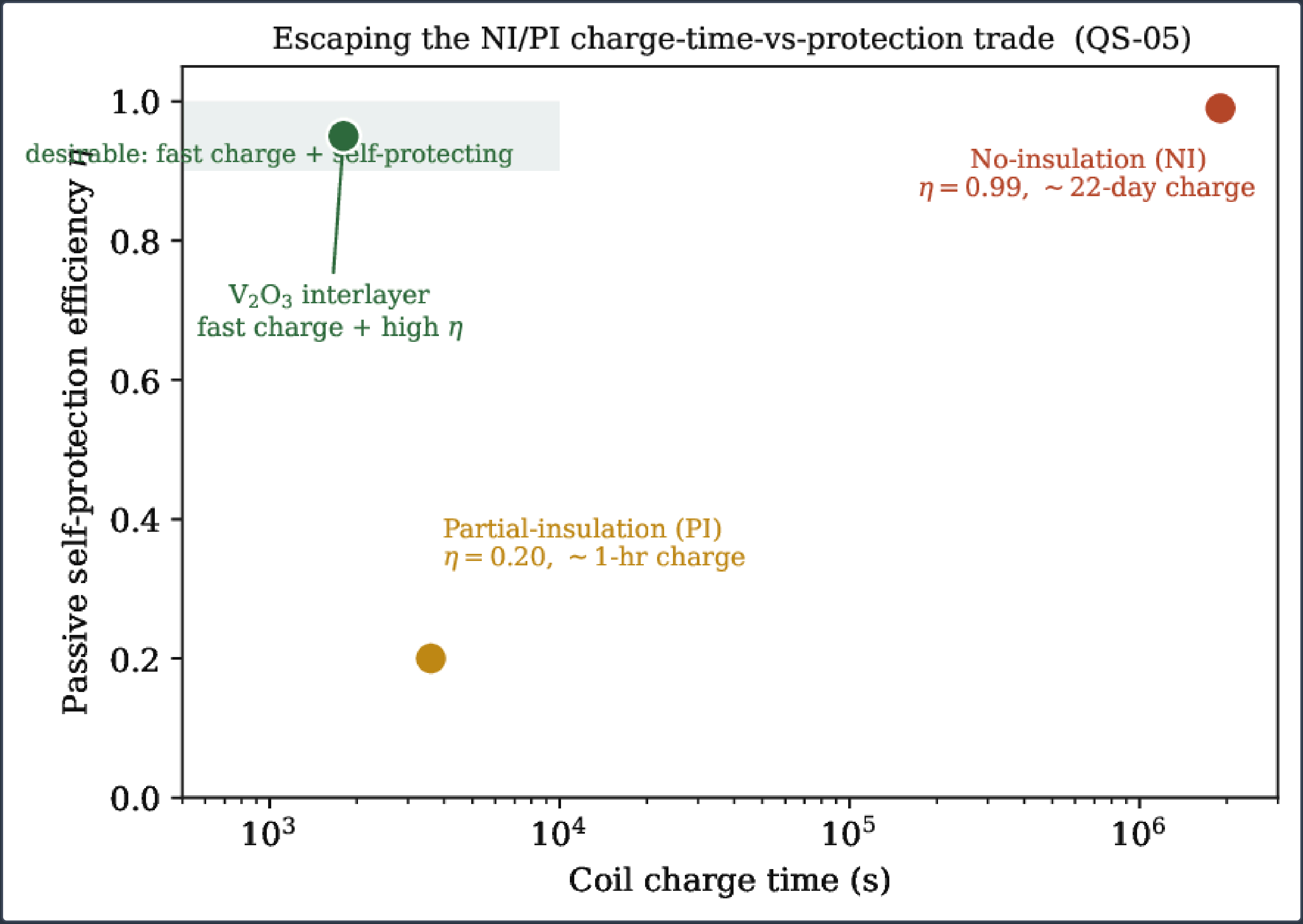

Escaping the no-insulation charge-time-versus-protection trade. No-insulation ($\eta = 0.99$, ~22-day charge) and partial-insulation ($\eta = 0.20$, ~ 1-hr charge) sit on the trade curve; the V_2O_3 interlayer reaches the desirable corner (QS-05[R0]).

The four materials results assemble into a single conductor architecture for the neutron-exposed centrepost, shown schematically in Fig. 8: an un-doped REBCO layer on a strain-first substrate for break-even-fluence lifetime, the V_2O_3 Mott interlayer for passive turn-to-turn self-protection, an operating-point-matched high-heat-capacity quench-margin layer, and the graphene-reinforced ultra-pure aluminium bypass stabiliser, with a functionalised-graphene interlayer arresting delamination (anchors Reg. #28/#29/#30/#10).

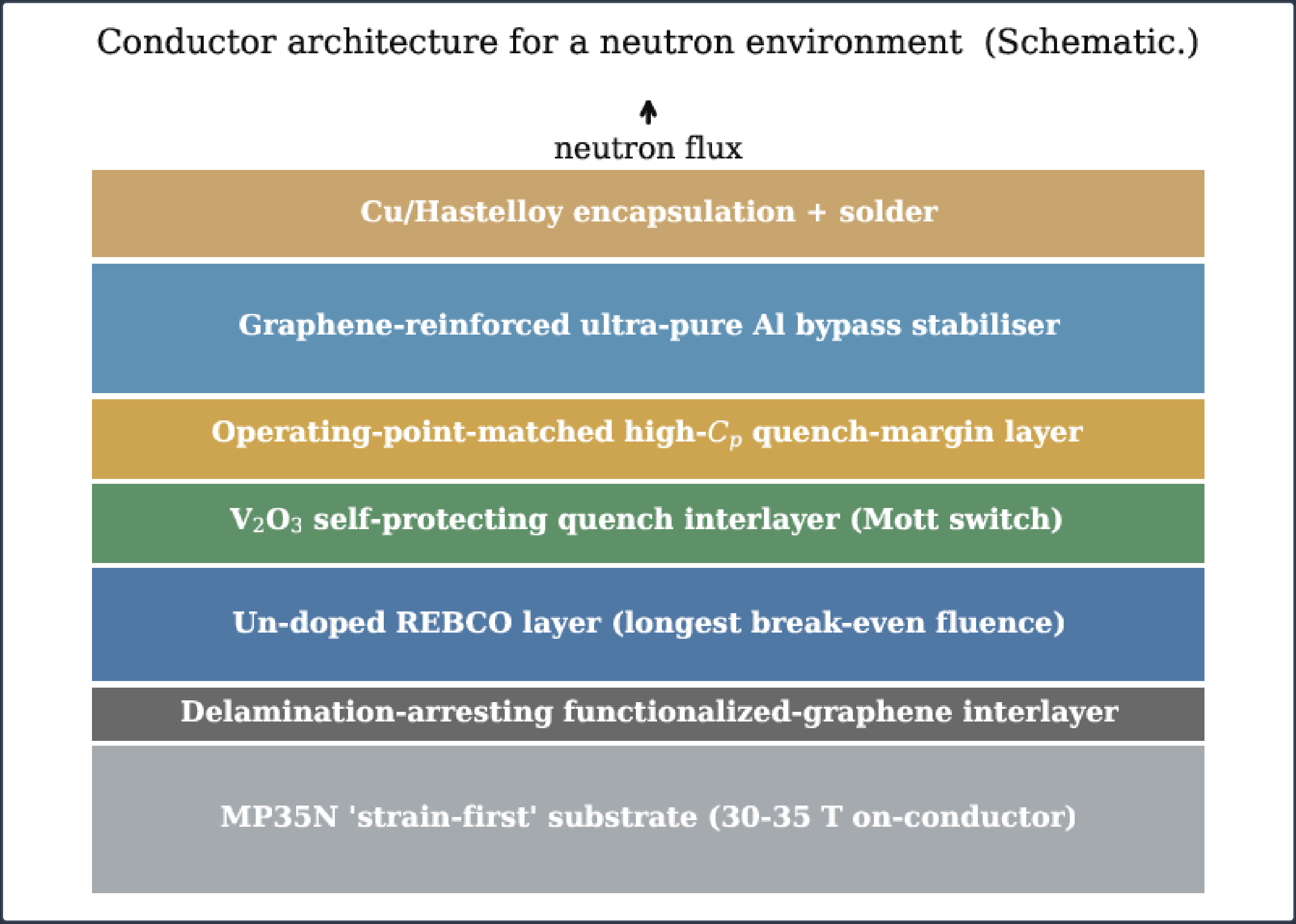

The conductor-materials architecture for a neutron environment, assembling the un-doped REBCO layer, V_2O_3 self-protecting interlayer, high-C_p quench-margin layer, graphene-reinforced aluminium stabiliser and delamination-arresting graphene interlayer (anchors Reg. #28/#29/#30/#10[R0]). (Schematic.)

THE QUENCH BUDGET CLOSES

Figure 9 shows the hot-spot temperature trajectory. The adiabatic MIITs integral of Eq. 13 gives a **3.67** s budget to reach the **200** K design cap with no dump (anchor BR-SX-14); the low REBCO normal-zone propagation velocity of **10.5** cm s^{-1} (**48**× below LTS, Eq. 14, anchor QS-02) is what makes voltage-tap detection too slow and a distributed precursor necessary. With a fused strain-rate and magnetisation precursor that fires **34**× earlier than terminal voltage (**0.089** s versus **3.02** s, SNR **323**; companion [2.19]), a **52** ms detection plus a **231** ms dump holds the peak temperature to **63** K (anchor QS-03), an order of magnitude below the cap. Table 1 collects the protection numbers. Table 2 summarises the paper's frozen anchors.

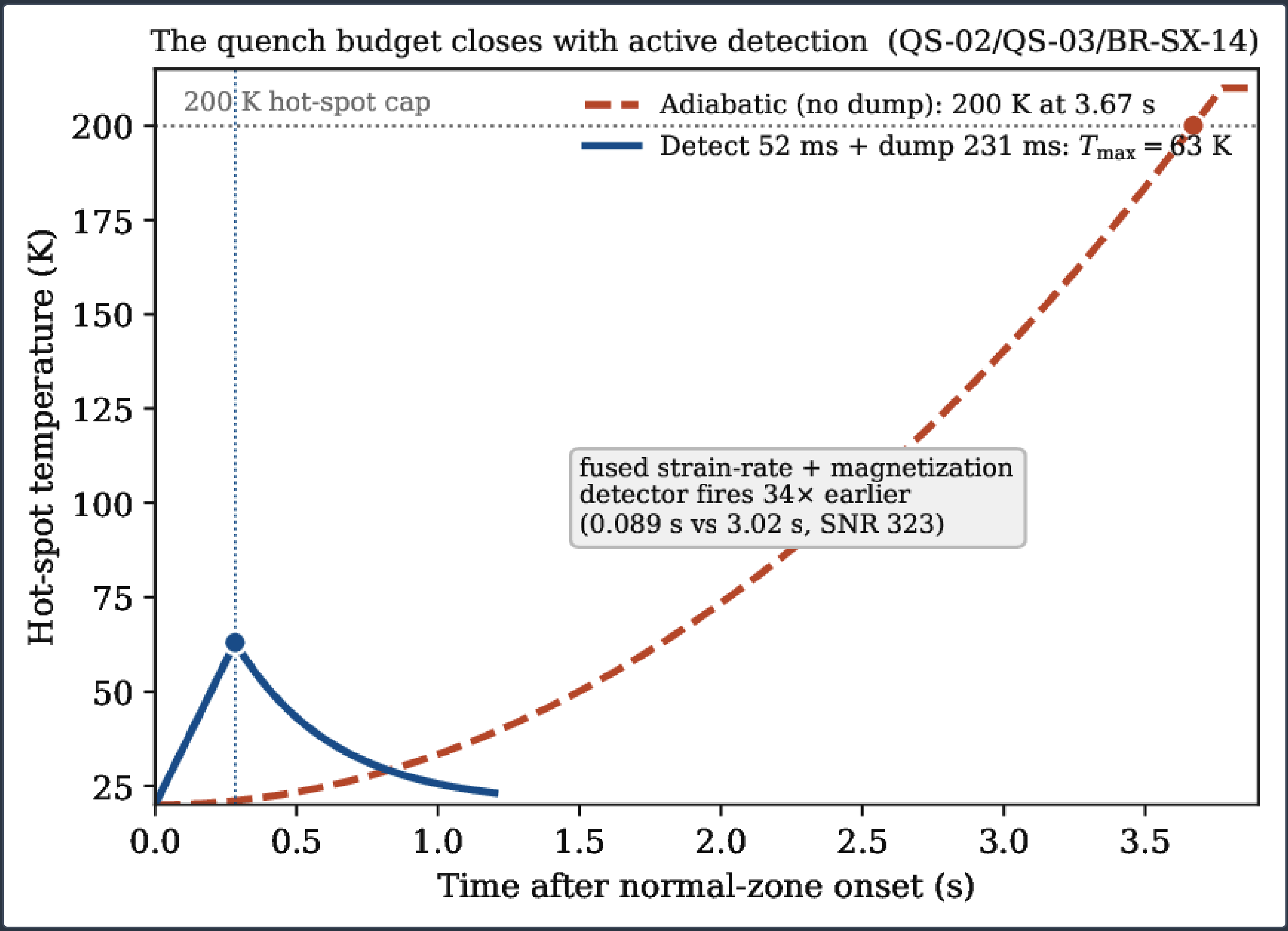

The quench budget closes with active detection. Adiabatically the hot spot reaches the **200** K cap in **3.67** s (BR-SX-14[R0]); with **52** ms detection and a **231** ms dump the peak is held to **63** K (QS-03[R0]). The fused precursor fires **34**× earlier than terminal voltage.

XLL QUANTITY	VALUE	SERIAL
Adiabatic hot-spot budget to 200 K	**3.67** s (**2.59** s at RRR 10)	BR-SX-14
MIITs integral $U(200\,\mathrm{K})$	9.9×10^{16} $A^2 s\, m^{-4}$	QS-03
Normal-zone propagation velocity	**10.5** cm s^{-1} (**48**× below LTS)	QS-02
Fused-precursor detection latency	**0.089** s (**34**× earlier than V; SNR **323**)	BR-SX-14
Detect + dump → peak temperature	**52** ms + **231** ms → **63** K	QS-03
NI self-protection efficiency / charge	$\eta = 0.99$ / ∼22 d	QS-05

table continued

PI self-protection efficiency / charge	$\eta = 0.20$ / $\sim$1 h	QS-05

XLLL RESULT	VALUE	FIG.	SERIAL
Un-doped break-even fluence	$5.64 \times 10^{22}\,\mathrm{n\,m^{-2}}$	1	BR-SX-04
APC break-even fluence	$3.82 \times 10^{22}\,\mathrm{n\,m^{-2}}$ ($\times$1.48)	1	BR-SX-04
Frozen design fluence budget	$3.9 \times 10^{22}\,\mathrm{n\,m^{-2}}$	1	register[R0]
Ordering robustness (4 000 samples)	$P = 1.00$	2	BR-SX-04
Oxygen-sublattice displacement share	$\approx 78\%$	3	BR-SX-04
DFT+U pristine YBCO cell energy	-2907.082 Ry	—	BR-SX-04
In-field margin at $3.9 \times 10^{22}\,\mathrm{n\,m^{-2}}$ (un-doped/APC)	1.23 / 1.80	4	BOM-03
Graphene–Al stabiliser conductivity (30–35 T)	$\sim 2 \times 10^{4}\,\mathrm{S\,cm^{-1}}$	5	Reg. #29
V_2O_3 Mott transition	≈ 160 K	6	Reg. #10

Conductor-materials frozen anchors reproduced in this paper.

§ 5

Discussion

Against the irradiation literature. The non-monotone $J_c(\Phi)$ of Eq. 6 — a low-dose rise from irradiation-added pinning followed by a damage-dominated fall — reproduces the qualitative behaviour reported in reactor and spallation campaigns on commercial REBCO tapes [8,9] and in light-particle surrogates that deliberately introduce pinning defects [10]. Our contribution is to make the *selection* between tape types quantitative and to invert the room-temperature ranking for the fusion-fluence regime: because the APC tape is engineered near pinning saturation, its available irradiation gain is small and its damage collapse arrives sooner, so it breaks even at 3.82×10^{22} against $5.64 \times 10^{22}\,\mathrm{n\,m^{-2}}$ for the un-doped tape. This is consistent with, and sharpens, the general observation that irradiation and artificial pinning are partly redundant.

The honest tension, resolved. Figure 4 shows the APC tape retaining more in-field margin at the operating field even though it broke even earlier. We do not paper over this. The resolution is that the two metrics answer different questions: break-even fluence answers “which tape keeps benefiting from irradiation longest,” relevant when the lifetime is set by a shield-limited fluence budget and the conductor is replaced on a cartridge cadence [2.26,2.16]; in-field margin answers “which tape has the most current headroom at end of life,” relevant when the operating field is pushed to the conductor limit. For the Hyperion centrepost at 16.84 T with a $3.9 \times 10^{22}\,\mathrm{n\,m^{-2}}$ shield-set budget, the un-doped-tape rule governs the lifetime and the margin figure sets the crossover field above which an APC lot is instead required — a design-space statement, not a contradiction. The register carries both anchors precisely so the coil designer can choose per operating point.

Against high-field magnet practice. The convergence of SPARC/ARC, the 45.5 T insert and VIPER-cable programmes on NI/PI winding [6,5,3] is driven by the same self-protection logic we formalise in §2.5; the V_2O_3 interlayer is a materials route to the self-protection benefit *without* the charge-time penalty, which is a genuinely different point in the design space than a fixed turn-to-turn contact resistance. The saturating-magnetoresistance argument for an aluminium bypass [20] is standard in cryomagnet stabiliser selection; the graphene reinforcement is what makes it structurally viable at 30–35 T. The quench-detection numbers are competitive with the HTS quench-detection literature [21,22,23]: the low REBCO NZPV that defeats voltage taps is exactly the regime those works target, and the fused precursor's $34\times$ earlier trigger is a meaningful margin in a deliberately hard, weak-signal regime.

Two distinct magnets. The centrepost (16.84 T) and the burner plug (26.49 T) are physically different coils with different fluence and stress environments; the conductor-materials specification here applies to the neutron-exposed centrepost, while the plug coil's structural and quench engineering is treated separately [2.21]. We are careful throughout not to conflate the two field values or their magnets.

§ 6

Limitations

The lifetime rule and the onset-knee surrogate are *screening* results anchored to available irradiation data, cascade molecular dynamics in the metallic layers, and a DFT+U energetics chain whose full chain-oxygen-vacancy and YBCO cascade extension are gated to the next HPC allocation; they are not a full reactor-irradiation qualification, and the break-even fluences carry the underlying data′s uncertainty (propagated in Fig. 2). The single honest gate is the same one flagged across the magnet programme [2.19]: an in-winding precursor sensor must survive a required tolerance of order $3.9 \times 10^{18}\,\mathrm{n\,cm^{-2}}$, roughly $39\times$ above the demonstrated $\sim 10^{17}\,\mathrm{n\,cm^{-2}}$, and that survival is not yet proven. The stabiliser conductivity target and the V_2O_3 transition parameters are material-property targets to be confirmed at winding scale. These materials define a conductor specification; they do not by themselves qualify a coil.

§ 7

Conclusion

In a fusion neutron environment the REBCO conductor specification changes. A two-population pinning model with a displacement-damage sink, anchored to cascade molecular dynamics and DFT+U, predicts that the un-doped tape outlasts the artificial-pinning-centre tape on break-even fluence (5.64×10^{22} versus $3.82 \times 10^{22}\,\mathrm{n\,m^{-2}}$, $\times 1.48$; ordering robust with probability 1.00 over $4\,000$ samples), inverting the room-temperature ranking, with the damage localised on the oxygen sublattice ($\approx 78\%$). A break-even-fluence surrogate screens candidate tapes without a full reactor campaign, and the in-field operating-point margin resolves the crossover to an APC lot honestly rather than by fiat. A graphene-reinforced ultra-pure aluminium stabiliser beats copper as a cryogenic bypass through its saturating magnetoresistance to 30–35 T, and a V_2O_3 Mott interlayer gives passive, temperature-triggered turn-to-turn quench protection that escapes the no-insulation charge-time trade. The quench budget closes with a 3.67 s adiabatic margin and a fused precursor firing $34\times$ early to hold the peak temperature to 63 K. This is the conductor-materials architecture behind the magnet, distinct from its field and stress design.

Acknowledgments tocsectionAcknowledgments Part of the Kronos Fusion Energy 2026 design series. The authors thank the Kronos physics de-risking programme for the frozen result set underlying every quantitative claim, and the NVIDIA GPU HPC campaign for the compute that produced the cascade-MD, DFT+U and Monte-Carlo results.

Reproducibility. Every headline quantity is a frozen anchor in the KRONOS Physics De-Risking Register, v8 [29] (doi:10.5281/zenodo.22133057): the un-doped/APC break-even fluences and ordering robustness (BR-SX-04), the in-field margin load line (BOM-03), the oxygen-sublattice partition (BR-SX-04), the quench budget (QS-02/QS-03/BR-SX-14/QS-05), and the stabiliser and V_2O_3 interlayer anchors (Reg. #29/#10). Each is regenerable from the deposited figure-generation script; this paper is archived at doi:10.5281/zenodo.22645779; official version: https://www.kronosfusionenergy.com/publications/rebco-conductor-materials-under-irradiation.html. No result depends on unpublished or proprietary data, and no economic analysis is part of this work.

Data availability tocsectionData availability The selection-rule curves, Monte-Carlo ordering distribution, sublattice partition, in-field margin load line, stabiliser magnetoresistance, V_2O_3 transition, NI/PI/V_2O_3 trade and quench budget of Figs. 1–9 are generated by the script deposited with this paper and archived at doi:10.5281/zenodo.22645779. All quantitative values trace to the register [29] (doi:10.5281/zenodo.22133057) by the serial identifiers cited inline. No economics appears in the public deposit.

Competing interests tocsectionCompeting interests Provisional patent applications relating to aspects of this work (the un-doped-tape selection rule, the graphene-reinforced stabiliser, and the V_2O_3 self-protecting interlayer) have been filed.

tocsectionReferences

APPARATUS

Portfolio, People & Record

The intellectual-property estate, the people who built it, the limitations that gate it, and the sources it rests on.

1	4	40	27
GRANTED PATENT	2026 PROVISIONALS	TEAM MEMBERS	2022 PROVISIONALS

INTELLECTUAL PROPERTY

The patent portfolio

The estate spans a granted high-field magnet patent, pending utility and 2026 provisional filings that map to the two products, a digital-twin control provisional, a registered trademark application, and the original 2022 provisional family. Every patentable disclosure in the five-paper arXiv drop was protected **before** publication: the breeder and burner provisionals were filed 1–2 August, and a publication-gap omnibus filing the evening before the drop swept up the DEC, plasma-control, and REBCO-winding matter of the three otherwise-unprotected papers. Patent numbers and application serials are matters of public record; claim scope is summarised, not reproduced.

GRANTED & PENDING UTILITY

US 12,009,112	High-field tilted graded-REBCO magnet architecture (KRONO-002A) · *app. 17/878,550*	GRANTED
US 17/878,507	Core device / method (KRONO-001A) · *utility*	PENDING

2026 PROVISIONAL FILINGS — MAPPED TO THE PRODUCTS

64/124,209	Hyperion — spherical-tokamak tritium / helium-3 foundry · *breeder · filed Aug 2026*	FILED
64/124,220	Aegis / MetroVolt — synchrotron-cutoff, fuel-selection & plug-winding · *generator · filed Aug 2026*	FILED
64/115,167	KRONOS-CTRL digital-twin plant control · *provisional · filed Jul 2026*	FILED
64/005,440	Integrated spherical-tokamak fusion architecture · *early integrated-architecture filing · filed Mar 2026*	FILED
64/105,530	Negative-triangularity spherical-tokamak architecture · *foundational ST filing · filed Jul 2026*	FILED
64/128,097	Publication-gap omnibus — quasineutral two-species expander DEC · provenance-gated / latency-split plasma control · as-built high-field winding & conductor architecture · *filed 7 Aug 2026, the evening before the arXiv drop*	FILED

TRADEMARK & ORIGIN

FTK-98801894	Kronos Fusion Energy — trademark application	FILED
KR-2022-*	Original provisional family (KR-2022-00001 … 00027) · *27 filings, 2022*	PRIORITY

The narrow, defensible magnet novelty — the specific conductor and the digital-twin winding optimisation, not high-field REBCO as a category — is the commercial core that can earn ahead of any Q > 1 milestone, with markets in fusion magnet supply, MRI/NMR, accelerators, and proton therapy. The claim is scoped honestly: the high field is a *system field* result, not a stand-alone-coil record; the small-bore plug coil is structurally infeasible as a bare winding but resolved by a stress-managed structural shield (feasible-pending-FEA); and the winding-tape experiment returned a *null result*. The value is the method, not a field record.

THE TEAM

Founding partners, board, advisors & auditors

Kronos is built by a bench of advanced-fuel-fusion, high-field-magnet, direct-conversion, and materials specialists, with a board and operations team drawn from defense, national laboratories, and industry. Dates are shown as ranges; where a tenure has ended or is term-ending, the range says so.

FOUNDING PARTNERS — SCIENCE

Dr. Gerald Kulcinski
Co-Founder · Helium-3 & Advanced-Fuel Fusion
UW–Madison · 2023–Present

Dr. Carl Weggel
Chief Scientist / S.M.A.R.T. Design
MIT Alcator Program · 2022–Present

Dr. Robert J. Weggel
Magnetic Field Design
MIT Magnet Lab · 2022–Present

BOARD

Priyanca Ford
Founder & CEO · Executive Board
2022–Present

Bandel Carano
Finance / Strategy
Oak Investment Partners / Stanford · 2025–2026

Patrick Schweiger
Fusion Device Engineering
Oklo / CFS / TerraPower · 2025–Present

SCIENTIFIC ADVISORS

Dr. Steven O. Dean
Fusion Policy & History
DOE / Fusion Power Associates · 2025–Present

Dr. Patrick H. Diamond
Plasma Turbulence & Transport
UC San Diego · 2025–Present

Dr. Jack J. Dongarra
HPC & Numerical Algorithms
Turing Award · 2025–Present

Dr. Nasr M. Ghoniem
Chief Material Scientist
UCLA · 2025–Present

Dr. Siegfried Glenzer
Plasma Physics & Laser Fusion
Stanford / SLAC · 2022–Present

Dr. David A. Hammer
Pulsed-Power Fusion
Cornell · 2025–Present

Dr. Donald A. Spong
Plasma Theory & Confinement
ORNL · 2025–Present

Dr. Curtis Smith
Risk Assessment & Nuclear PRA
MIT / Idaho National Lab · 2025–Present

RADM (Ret.) David Goggins
Naval Engineering & Power-Plant Design
U.S. Navy · 2023–2026

Dr. Konstantin Batygin
Mathematician
Caltech · 2022–2025

Dr. Ruben Fair
Magnet Design / ITER Liaison
PPPL / Jefferson Lab · 2022–2025

Dr. Paul S. Weiss
Materials & Nanotechnology
UCLA · 2022–2025

SCIENTIFIC AUDITORS

Dr. Wilfred A. Cooper
Plasma Equilibrium Theory
EPFL / Swiss Plasma Center · 2025–Present

Dr. Ahmed Hassanein
Plasma–Material Interactions
Purdue / Argonne · 2025–Present

Dr. Patrick E. Hopkins
Extreme Thermal Materials
U. of Virginia · 2025–Present

Dr. Peter Hosemann
Materials Joining & Structural Integrity
UC Berkeley · 2025–Present

Dr. Travis W. Knight
Advanced Nuclear Fuels & Systems
U. of South Carolina · 2025–Present

Dr. Philippe Lebrun
Cryogenics & Magnet Cooling
CERN · 2025–Present

Dr. Nitendra Singh
Nuclear Safety & Fuel Cycle
ITER · 2025–Present

Dr. Guido Van Oost
Magnetic Confinement & Fusion Systems
Ghent University · 2025–Present

Dr. Gary S. Was
Radiation Materials & Structural Integrity
U. of Michigan · 2025–Present

Dr. Ray Sedwick
Direct Energy Conversion
U. of Maryland · 2025

OPERATIONS

Michael Laughlin
Chief Operating Officer
2022–Present

Martin Owens
Chief Strategy Officer
LANL / GE Hitachi · 2022–Present

MG (Ret.) Paul Pardew
Chief Contracting Officer
Army Contracting Command · 2022–Present

David Beck
Fusion Commercialization
U.S. Space Force · 2024–Present

Sushma Bhatia
Environmental & Legislative
Google · 2022–Present

Michael De Frenza
Technology Licensing
2023–Present

MG (Ret.) Robin L. Fontes
Cybersecurity & Defense
Army Cyber Command · 2022–Present

Vijay Gehani
Supply Chain & Components
INOX India · 2024–Present

Jon Michel Greenwood
IT & AI Infrastructure
Live Nation · 2023–Present

Brian C. O'Neill
National Security
CIA / ODNI · 2022–Present

Gen. (Ret.) Gustave F. Perna
DoD Liaison
Operation Warp Speed · 2022–2023

Andrea Romero
Marketing Lead
2022–Present

Legal counsel is retained; those roles are held on the internal roster and are not listed here.

SOURCES

References

1 J E Menard *et al*, Fusion nuclear science facilities and pilot plants based on the spherical tokamak, *Nucl. Fusion* **56** 106023 (2016). doi:10.1088/0029-5515/56/10/106023

2 B N Sorbom *et al*, ARC: a compact, high-field, fusion nuclear science facility and demonstration power plant with demountable magnets, *Fusion Eng. Des.* **100** 378 (2015). doi:10.1016/j.fusengdes.2015.07.008

3 A J Creely *et al*, Overview of the SPARC tokamak, *J. Plasma Phys.* **86** 865860502 (2020). doi:10.1017/S0022377820001257

4 J L MacManus-Driscoll and S C Wimbush, Processing and application of high-temperature superconducting coated conductors, *Nat. Rev. Mater.* **6** 587 (2021). doi:10.1038/s41578-021-00290-3

5 S Hahn *et al*, 45.5-tesla direct-current magnetic field generated with a high-temperature superconducting magnet, *Nature* **570** 496 (2019). doi:10.1038/s41586-019-1293-1

6 S Hahn, Y Kim, D K Park, K Kim, J P Voccio, J Bascu\ n\'an and Y Iwasa, No-insulation multi-width winding technique for high temperature superconducting magnet, *Appl. Phys. Lett.* **103** 173511 (2013). doi:10.1063/1.4826217

7 A Molodyk *et al*, Development and large volume production of extremely high current density YBCO superconducting wires for fusion, *Sci. Rep.* **11** 2084 (2021).

8 D X Fischer *et al*, The effect of fast neutron irradiation on the superconducting properties of REBCO coated conductors with and without artificial pinning centers, *Supercond. Sci. Technol.* **31** 044006 (2018). doi:10.1088/1361-6668/aaadf2

9 M Eisterer, Radiation effects on the critical current density of high-temperature superconductors, review chapter in *Handbook of Superconductivity* (2018).

10 M Leroux *et al*, Rapid doubling of the critical current of $YBa_2Cu_3O_{7-\delta}$ coated conductors for viable high-speed industrial processing, *Appl. Phys. Lett.* **107** 192601 (2015).

11 M J Norgett, M T Robinson and I M Torrens, A proposed method of calculating displacement dose rates, *Nucl. Eng. Des.* **33** 50 (1975).

12 K Nordlund *et al*, Improving atomic displacement and replacement calculations with physically realistic damage models, *Nat. Commun.* **9** 1084 (2018).

13 S Plimpton, Fast parallel algorithms for short-range molecular dynamics, *J. Comput. Phys.* **117** 1 (1995).

14 A P Thompson *et al*, LAMMPS — a flexible simulation tool for particle-based materials modeling at the atomic, meso, and continuum scales, *Comput. Phys. Commun.* **271** 108171 (2022).

15 P Giannozzi *et al*, QUANTUM ESPRESSO: a modular and open-source software project for quantum simulations of materials, *J. Phys.: Condens. Matter* **21** 395502 (2009).

16 S L Dudarev, G A Botton, S Y Savrasov, C J Humphreys and A P Sutton, Electron-energy-loss spectra and the structural stability of nickel oxide: an LSDA+U study, *Phys. Rev. B* **57** 1505 (1998).

17 P K Romano, N E Horelik, B R Herman, A G Nelson, B Forget and K Smith, OpenMC: a state-of-the-art Monte Carlo code for research and development, *Ann. Nucl. Energy* **82** 90 (2015). doi:10.1016/j.anucene.2014.07.048

18 F J Morin, Oxides which show a metal-to-insulator transition at the N\'eel temperature, *Phys. Rev. Lett.* **3** 34 (1959).

19 M Imada, A Fujimori and Y Tokura, Metal-insulator transitions, *Rev. Mod. Phys.* **70** 1039 (1998).

20 F R Fickett, Magnetoresistance of very pure polycrystalline aluminum, *Phys. Rev. B* **3** 1941 (1971).

21 M Marchevsky, Quench detection and protection for high-temperature superconductor accelerator magnets, *Instruments* **5** 27 (2021). doi:10.3390/instruments5030027

22 E E Salazar *et al*, Fiber optic quench detection for large-scale HTS magnets demonstrated on VIPER cable during high-fidelity testing at the SULTAN facility, *Supercond. Sci. Technol.* **34** 035027 (2021). doi:10.1088/1361-6668/abdba8

23 R Teyber, J Weiss, M Marchevsky, S Prestemon and D van der Laan, Current distribution monitoring enables quench and damage detection in superconducting fusion magnets, *Sci. Rep.* **12** 22502 (2022). doi:10.1038/s41598-022-26592-3

COLOPHON

How this document was made

The Kronos Fleet — Combined Editorial, 2026 is set in **Fraunces** (display), **Gelasio** (text), and **IBM Plex Mono** (data & equations), carried forward from the Kronos editorial design system.

The figures are rendered at 300 dpi from the deposited generator scripts; the document is composed as a single self-contained file with embedded fonts and imagery, paginated to US Letter, and rendered to PDF through a headless Chromium engine in matched light and dark editions.

Every headline quantity carries an evidence class; withdrawn and restated values are marked as such. Nothing herein is frozen beyond the founder-approved Tier-A set.

Explore it live — turn the interactive 3-D model, run the deposited solvers in the physics validator, and watch the companion film series.

LEGAL NOTICE

Notice, status, and distribution

Conceptual design & simulation study. This document reports a conceptual design and simulation study. It is not a construction commitment, a safety-analysis report, a regulatory filing, or an offer of securities. Forward-looking statements — schedules, costs, market sizes, and performance — are estimates subject to the limitations set out in the Simulations part and may change.

Numbers and their classes. Quantities are reported with evidence classes and case labels; modelled, assumed, and requirement-class values are identified as such and are not to be quoted without their labels.

Public edition. This edition carries the physics and design only; all financial, funding, and defense-commercial content has been removed for public distribution. The scientific text corresponds to the arXiv and journal submissions.

THE 2026 KRONOS SERIES

One programme, many papers

This editorial is one paper in the Kronos 2026 series — a real fusion company's complete, reproducible physics record for a spherical-tokamak breeder and its low-neutron D–^{3}He tandem-mirror burners. Every headline number is a frozen anchor in the Physics De-Risking Register.

Explore the whole programme: the De-Risking Register, the interactive 3-D model, and the physics validator.

KRONOS FUSION ENERGY

REBCO Conductor and Stabilizer Materials Under Neutron Irradiation: The Un-Doped-Tape Rule, Graphene-Reinforced Stabilizers and V2O3 Self-Protection for a Spherical-Tokamak Breeder

A real fusion company building real machines. Explore the science, live.

Zenodo · doi:10.5281/zenodo.22645779

Read on kronosfusionenergy.com

The Physics De-Risking Register